Pulsed electric current joining of oxide-dispersion-strengthened austenitic steels

Fei Wang[a], Xueliang Yan[a], Xin Chen[a], Nathan Snyder[a], Michael Nastasi[b], Khalid Hattar[c], Bai Cui[a,d,†]

[a] *Department of Mechanical and Materials Engineering, University of Nebraska-Lincoln, Lincoln, NE 68588, USA*

[b] *Department of Nuclear Engineering, Texas A&M University, College Station, TX 77843, USA*

[c] *Center for Integrated Nanotechnologies, Sandia National Laboratories, Albuquerque, NM 87185, USA*

[d] *Nebraska Center for Materials and Nanoscience, University of Nebraska-Lincoln, NE 68588, USA*

[†] Corresponding author. Tel.: +1 (402) 472-5740; fax: +1 (402) 472 1465; email: bcui3@unl.edu.

Abstract

The solid-state joining of oxide-dispersion-strengthened (ODS) austenitic steels was realized using a pulsed electric current joining (PECJ) process. Microstructures of the austenitic grain structures and oxide dispersions in the joint areas were characterized using electron microscopy. Negligible grain growth was observed in austenitic grain structures, while slight coarsening of oxide dispersions occurred at a short holding time. The mechanisms of the PECJ process may involve three steps that occur simultaneously, including the sintering of mechanical alloying powders in the bonding layer, formation of oxide dispersions, and bonding of the mechanical alloying powders with the base alloy. The high hardness and irradiation resistance of ODS alloys were retained in the joint areas. This research revealed the fundamental mechanisms during the PECJ process, which is beneficial for its potential applications during the advanced manufacturing of ODS alloys.

Keywords: oxide-dispersion-strengthened alloys; pulsed electrical current joining; joining; austenitic steels

1. Introduction

Oxide-dispersion-strengthened (ODS) alloys are promising materials to meet the demand of advanced nuclear applications due to high-temperature stability, corrosion resistance, excellent mechanical strength, creep resistance, and radiation tolerance [1–4]. ODS ferritic steels have been prevalently investigated for Generation-IV nuclear power systems, leading to the development of many alloys such as 14Cr ODS, 14YWT, MA956, MA957, and PM2000 [5–8]. ODS austenitic steels (e.g., ODS 316, ODS 304) have been recently developed for nuclear energy applications in very-high-temperature reactors (VHTR) and advanced fossil energy systems [9–11]. ODS austenitic steels have better creep resistance than ferritic steels, because the close-packed face-centered cubic (FCC) structure is more stable and more resistant to creep than the body-centered cubic (BCC) structure at high temperatures. The outstanding properties of ODS alloys originate from the homogeneous dispersion of oxide nanoparticles, including Y-Ti-O (Y_2TiO_5 and $Y_2Ti_2O_7$) or Y-Al-O ($YAlO_3$, $Y_2Al_2O_9$, and $Y_5Al_3O_{12}$), due to their high thermal stability [12, 13]. These oxide dispersions can effectively pin the dislocations and reduce grain coarsening, and trap radiation-induced defects and helium atoms at the dispersion/matrix interfaces [14–17].

A reliable joining or welding technique is very important for the practical application of ODS alloys as structural components in nuclear and fossil energy systems. Several joining and welding methods have been applied to ODS steels before. Wright *et al.* reviewed the prior work on joining/welding technologies of ODS alloys, such as tungsten inert gas welding, brazing bonding, transient liquid phase bonding, diffusion bonding, and friction stir welding [18]. It suggested that the unique nanostructure of dispersion particles was difficult to maintain in ODS alloy joints using existing joining technologies because they can generate excessive heating, melting, and solidification to disrupt the microstructures in the joint or heat-affected zone (HAZ). For example, the fusion welding processes (including tungsten inert gas, arc welding, laser welding, and electron beam welding) melt and re-solidify the joint region, resulting in the agglomeration and coarsening of dispersion particles, grain growth, and pore formation from the entrapped or absorbed gas [19–22]. Friction stir welding (FSW) has benefits such as the absence of melting or solidification, low distortion of the workpiece, and good dimensional stability [23, 24]. Nevertheless, Baker *et al.* report that FSW of MA 956 causes significant oxide particle coarsening due to a combination of Ostwald ripening and continued phase transformation within the Al_2O_3-Y_2O_3 system [25]. Similarly, the studies on PM 2000 concluded that FSW caused oxide particles to grow in the vicinity of the stir zones consisting of coarsened and equiaxed grains [24, 25]. Capacitive discharge resistance welding has been recently developed for ODS alloy cladding, which has rapid thermal cycles to form thinner weld zones than conventional techniques, although a thin recrystallization region was observed [26]. Therefore, the development of a reliable joining/welding technology remains a major technical challenge for nuclear and fossil applications of ODS alloys.

A pulsed electric current joining (PECJ) process has emerged as a promising approach that can produce an outstanding solid-state ODS ferritic alloy joint with minimal change of oxide dispersion [27, 28]. The PECJ process involves simultaneously applying a pulsed electric current and a uniaxial pressure to mechanical alloyed powders placed between two ODS alloy parts, producing a solid-state bonding (**Figure 1**). The mechanical alloyed powders have the same chemical composition as the ODS base alloy. Under the pulsed electric current and pressure, the mechanical alloying powders are consolidated (sintered) to form a bonding layer between ODS alloy parts. Because the PECJ process avoids the melting or excessive heating of ODS alloys, it will result in minimal changes in microstructures of oxide dispersions in ODS alloy joints.

Nishimoto, *et al.*, first applied the PECJ technique to join MA956 (with oxide dispersion particles of 24 nm) by inserting mechanical alloying powders (with particle size of 65 to 240 um) with the same composition with MA 956 between two metal rods, and forming a bonding layer at 750-1142 °C for up to 18 min in a vacuum atmosphere at a uniaxial pressure of 40-70 MPa [27]. The creep-rupture strength of the joined MA956 samples can retain 70% of the strength of the base metal. Tatlock, *et al.* demonstrated the successful joining of as-extruded PM 2000 rods (19 mm diameter) by a PECJ process at 1170-1380 °C in an Argon atmosphere at a pressure of 40-70 MPa perpendicular to the joint [28]. The joined PM 2000 samples exhibited a creep-rupture strength of 72-74% of the base metal at 1000 °C. Fu et al. [29]reported dissimilar joints between 9Cr-ODS and JLF-1 steels by hot isostatic pressing (HIP) and electron beam welding at 1000 to

1100 ºC for 3 hours under a pressure of 191 MPa. Compared to HIP, the advantage of PECJ is the much shorter time (10 min vs. 3 h) needed to complete the joining process. These prior studies indicate the potential of the PECJ process to maintain the superior mechanical properties of ODS ferritic steels at high temperatures. However, the previous research was limited to the ferritic ODS steels and no research on the PECJ process of ODS austenitic steels was reported. In addition, the fundamental mechanisms during the PECJ process, in particular the formation mechanisms of microstructures in the joint, were not well understood,

In this manuscript, ODS 304 austenitic steels were successfully joined using the PECJ process. Microstructures in the ODS alloy joints were characterized by scanning electron microscope (SEM), electron backscatter diffraction (EBSD), and transmission electron microscopy (TEM). The local mechanical properties were evaluated by the measurement of hardness along the cross-section of joints, and the stability of microstructures in irradiation environments was examined in the *in situ* ion irradiation transmission electron microscope (I^3TEM). These studies revealed the microstructure-property relationship in the PECJ joints, which aids understanding of the fundamental mechanisms of the PECJ process and is beneficial for its potential applications during advanced manufacturing of ODS alloys.

2. Experimental

ODS 304 austenitic steel samples were fabricated following the procedures in our previous paper [3]. Briefly, raw powders with a nominal composition of Fe-18%Cr-8.5%Ni-2%W-0.5%Ti-0.35%Y_2O_3 (wt.%) were ball milled at 250 rpm for 50 h in a high-energy planetary mill under an argon atmosphere. Consolidation of the mechanical alloying powders was achieved at 1000 °C for 5 min and applied uniaxial pressure of 50 MPa under vacuum.

ODS 304 austenitic steel samples for the PECJ process had a diameter of 20 mm and a thickness of ~1 mm. The surface was polished with SiC paper successively from 400 to 1200 grit. The PECJ process of ODS 304 austenitic steels was performed using the spark plasma sintering system (SPS, Model 10-4, Thermal Technology LLC) under vacuum (2×10^{-2} Torr). A schematic diagram of the PECJ process was illustrated in **Fig. 1**, in which two ODS steel samples were placed abutted, and a layer of mechanical alloying powders with the same chemical composition as the ODS steels was placed between them. The mechanical alloying powders were prepared by ball milling of element powder mixtures with a nominal composition of Fe-18%Cr-8.5%Ni-2%W-0.5%Ti-0.35%Y_2O_3 (wt.%) under an inert atmosphere at 250 rpm for 50 h using the planetary ball mill. The SPS system included a direct current (DC) power that provided a pulsed electric current with an electric voltage of 0 to 10 V, an electric current of 0 to 2000 A, and a pulse duration of 3 milliseconds to 1 second. The temperature of the powders was measured using three Type K thermocouples (maximum 1200 °C) and one optical pyrometer (450 to 3000 °C). The uniaxial pressure (0 to 50 MPa) was applied using the hydraulic load in the SPS system.

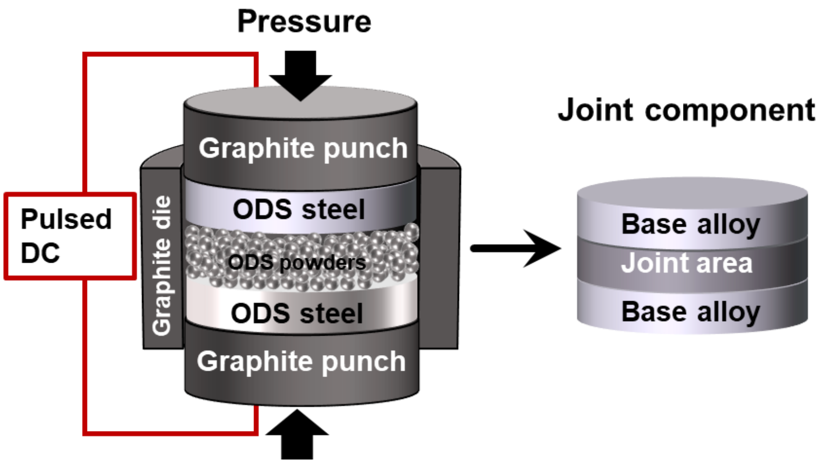

Fig. 1. The schematic diagram of the pulsed electric current joining (PECJ) process of ODS alloys.

After the PECJ process, the joined samples were machined and mechanically polished to reveal the cross-section microstructures. The sample surface was electrochemical polished in a solution of 5% $HClO_4$ and 95% C_2H_5OH. SEM and EBSD analysis were conducted in a FIB/SEM dual-beam workstation (Helios 660, FEI) equipped with an EBSD detector (Hikari XP 2, AMETEK) with a step size of 0.01 μm. During TEM sample preparations, disks in 3 mm diameter were punched out and thinned to a thickness of less than 100 μm by mechanical polishing. Final thinning to electron transparency was conducted by electrochemical polishing in a twin jet polisher using a solution of 5% $HClO_4$ and 95% CH_3OH at -20 °C. TEM characterizations were performed in a FEI Tecnai Osiris S/TEM operated at 200 kV using the bright-field (BF) imaging modes and energy-dispersive spectrometry (EDS) for chemical analysis. The Vickers hardness was measured using a hardness tester (Tukon 2500, Wilson) with a load from 3 N and a dwell time of 10 seconds.

The *in situ* ion irradiation experiments were carried out at the *in situ* ion irradiation TEM (I^3TEM) facility at Sandia National Laboratories [30]. TEM samples of PECJ joints were irradiated by 2.8 MeV Au^{4+} ions at room temperature with a current density of 1.15×10^{-3} Am^{-2} producing a damage rate of 1.32×10^{-3} dpa s^{-1}. The accelerated Au^{4+} ions bombarded the TEM sample at an incident angle of about 60°. The ion beam size was 3 mm, which can cover the whole TEM sample. Displacements per atom (dpa) were calculated by the Stopping and Range of Ions in Matter (SRIM) simulation by the Kinchin-Pease model following the recommendations by Stoller *et al.* [31]. Under these irradiation conditions, a fluence of 1.36×10^{18} ions m^{-2} can cause a damage level of about 1 dpa. The accuracy of the dose level is ±10%.

3. Results and discussion

Fig. 2 is a typical profile of the electrical voltage, current, and temperature during the PECJ process of 304 austenitic steels. An initial pulse of electrical voltage/current at t=2.5 min was used to start the Joule heating process, which was then almost linearly increased to provide a high heating rate of 100 ºC/min. When the temperature reached 1000 ºC and holding for 3 min, the electrical voltage/current was gradually decreased during the sintering process of mechanical alloying powders, because the output of electrical current was just needed to maintain the temperature at 1000 ºC instead of heating the sample. Then the voltage/current was decreased and stopped to allow the cooling rate of 100 ºC/min. It is noted that the relationship between electrical voltage and current followed the same trend, but their ratio was fluctuating that indicated changes of the electrical resistance of the system. The electrical resistance of this system (Fig. 1) consists of the resistance from the ODS steel sample, steel hydraulic ram, graphite molds, and the contact resistance between powder particles and that between the electrodes (i.e., ODS alloy part) and particles. The electrical resistance decreases during the sintering process and reaches lowest level when the temperature is 1000 ºC. The electrical resistance decrease is contributed by several factors, including the decrease of electrical resistance of graphite molds with temperature [32], lower resistance due to the sintering of particles (e.g., neck formation) [33], and lower contact resistance when the applied pressure increased from 25 to 50 MPa at 1000 ºC.

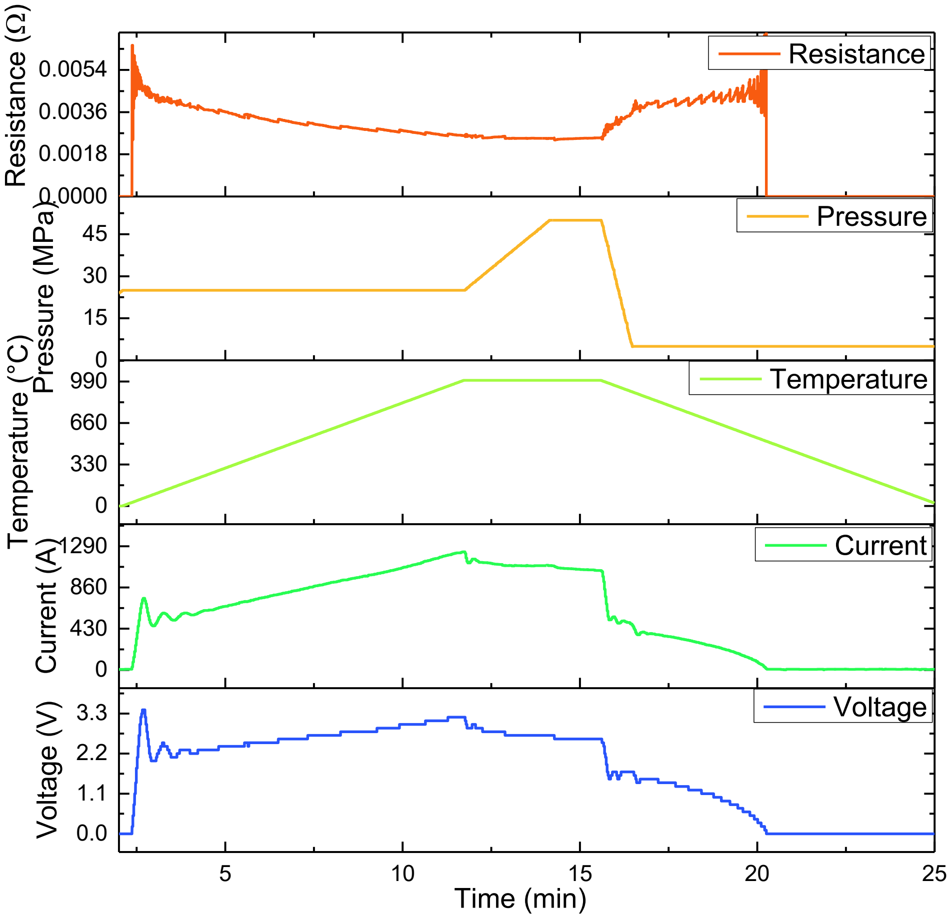

Fig. 2. The profiles of electrical voltage, current, resistance, pressure, and temperature during the PECJ process.

Fig. 3a and **3b** show the SEM images of the cross-section of the PECJ sample with holding time of 3 min and 10 min, respectively, at 1000 ºC. The red arrows indicated the location of the interfaces between the base alloy and the joint area. **Fig. 3a'** and **3b'** are the enlarged view of the boundaries in **Fig. 3a** and **3b**, respectively. There was no obvious microstructural difference between the joint area and base alloy, and no pores or cracks were observed in the joint area. The location of the interfaces are difficult to observe in the SEM images because there were no defects or impurities at the interfaces. These results suggested that an excellent solid-state bonding was formed by the PECJ process.

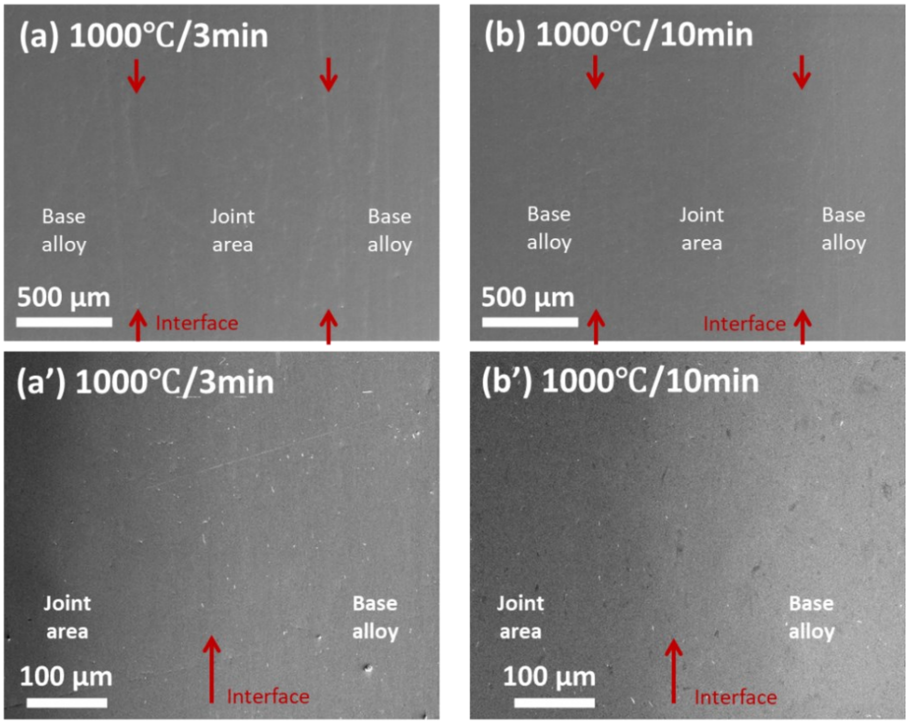

Fig. 3. SEM images of the cross-section of the PECJ samples of ODS 304 austenitic steels prepared at 1000 ºC and 50 MPa with a holding time of (a) 3 min and (b) 10 min. The vertical red arrows indicate the interfaces between the base metal and the joint. (a') and (b') are the enlarged view of the interface in (a) and (b), respectively.

EBSD analysis was conducted to examine the austenite grain size and orientation in the base alloy and joint areas of ODS 304 austenitic steel samples after the PECJ process. **Fig. 4a to 4c** are inverse pole figures of the austenitic grain structure that shows no preferred crystallographic orientation, while the grain size distributions of each image are presented in **Fig.**

4d to **4f**. Considering the statistic errors, there was no significant difference in the average grain size of the base alloy (618 ± 324 nm), the joint area with a holding time of 3 min (568 ±249 nm), and the joint area with a holding time of 10 min (643 ± 258 nm). However, the average grain size of the joint area appeared to increase slightly with the longer holding time (10 min vs. 3 min). These results generally suggest that grain growth was suppressed during the PECJ process, which may be attributed to the high heating and cooling rates (100 ºC/min). The large grain size variation may be attributed to the particle size variation of the ball milled powders (2.989±0.532 µm). Considering of the possibility of more Joule heating at the interface between joint and base alloy due to contact resistance, the grain size at the interface between joint and base alloy was analyzed by EBSD. The interface region of the 1000 ºC/3 min and 1000 ºC/10 min joint samples have grain size of 769±198nm and 815± 253nm, respectively, which is slightly larger than that of the joint area. This indicates more Joule heating in the interface region, but the difference between interface and joint area is not significant. There may be more Joule heating at the interface at the beginning stage of the PECJ process but this difference will diminish with the more soaking time when the interface region is sintered together with the powders resulting in decrease of the contact resistance.

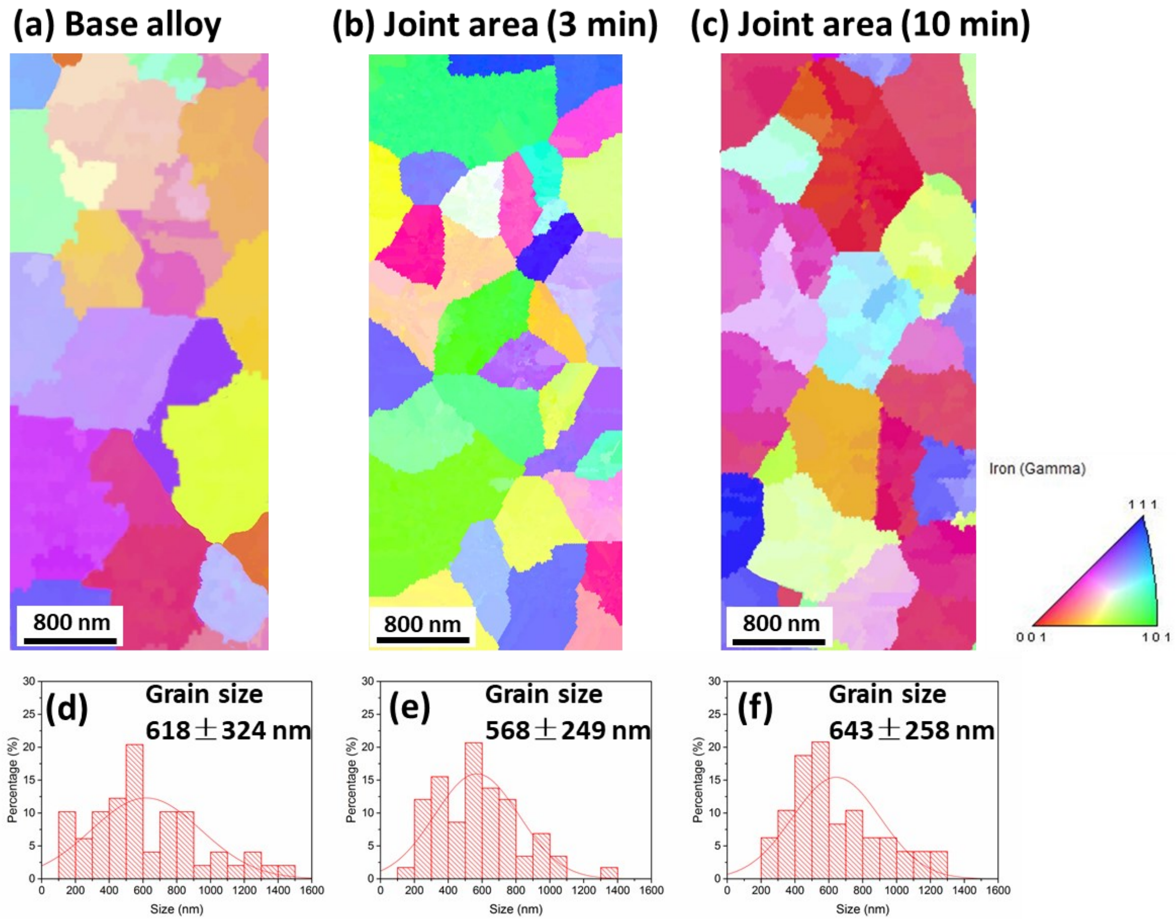

Fig. 4. Typical EBSD images of (a) base alloy and the joint area with a holding time of (b) 3 min and (c) 10 min. (d)-(e) are grain size distributions corresponding to a to c, respectively.

TEM characterizations were performed to analyze the potential coarsening and agglomeration of oxide dispersions in the joint areas of ODS 304 austenitic steels. TEM micrographs showed that the oxide dispersions remained uniformly distribution in both base alloy (**Fig. 5a**), the joint area with a holding time of 3 min (**Fig. 5b**), and the joint area with a holding time of 10 min (**Fig. 5c**). The particle size and number densities of oxide dispersions in the base alloy and joint areas were measured from the TEM images (**Fig. 5d** to **5f**). The average particle size of oxide dispersions in the base alloy (7.6 ± 7.2 nm) was similar to that in the joint area with a holding time of 3 min (8.1 ± 5.4 nm). However, the average particle size of the oxide dispersions increased more significantly from the holding time of 3 min to 10 min (13.3 ± 11.2 nm). The number density decreased from the $(8.7 \pm 1.3)\times10^{20}$ m^{-3} in the base alloy to $(6.6 \pm 0.2)\times10^{20}$ m^{-3} and $(4.8 \pm 1.2)\times10^{20}$ m^{-3} in the joint area with a holding time of 3 and 10 min, respectively. The larger size and lower number density of oxide dispersions in the joint areas suggested the coarsening of oxide dispersions occurred slightly after a short holding of 3 min but significantly after a longer holding time of 10 min. **Fig. 5g** shows the EDS analysis of the element distribution in an oxide dispersion particle, which is composed of Y, Ti, and O. This is consistent with the previous studies of ODS 304 austenitic steels, in which the oxide dispersions were Y–Ti–O oxide phase (presumably $Y_2Ti_2O_7$ and Y_2TiO_5) [3, 12].

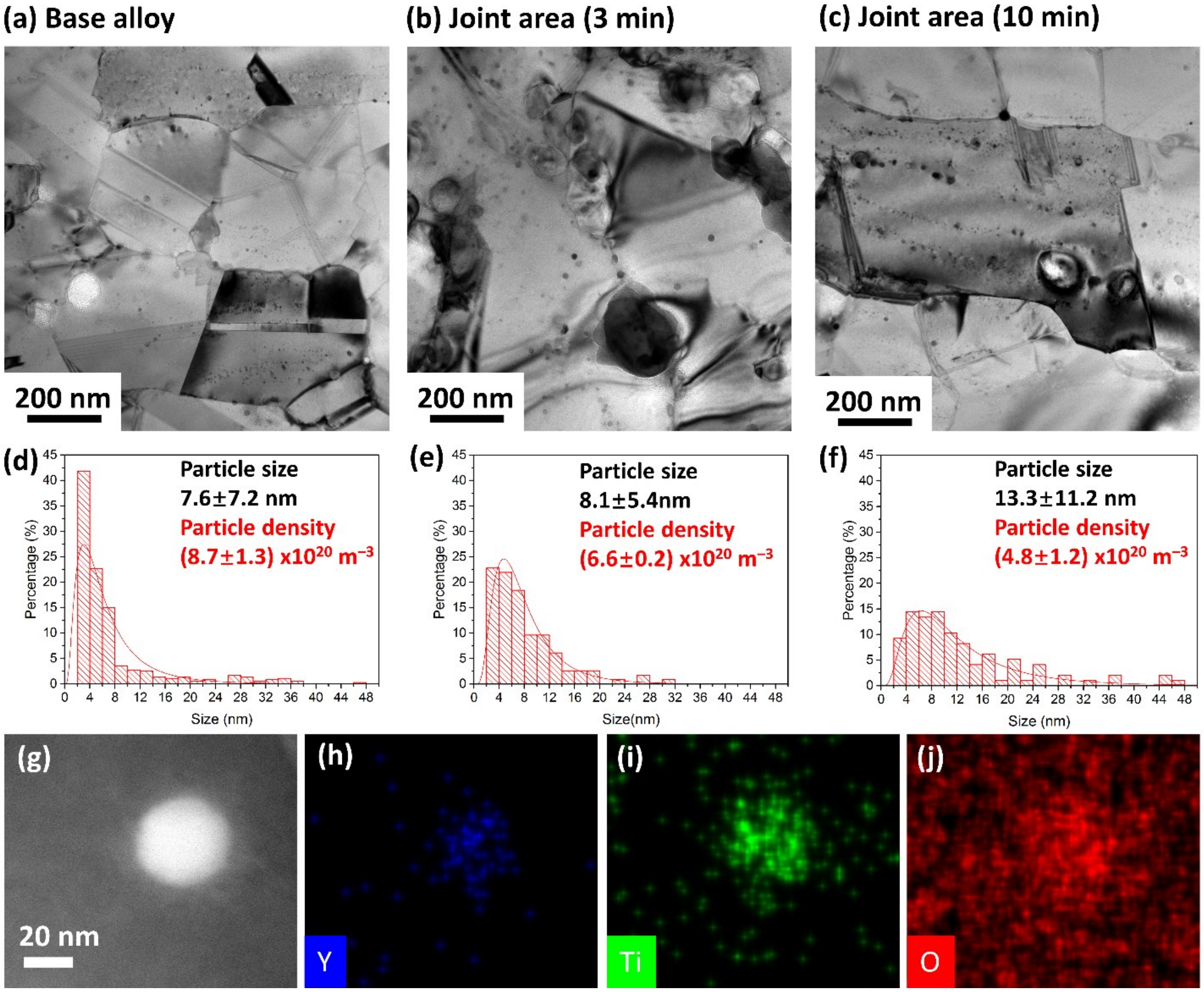

Fig. 5. Representative bright-field TEM images of (a) base alloy and the joint areas with a holding time of (b) 3 min and (c) 10 min. (d)-(f) are the quantitative analysis of the particle size distribution and number densities of oxide dispersions corresponding to images a to c, respectively. (g) HAADF image of an oxide dispersion particle. (h)-(j) elements distribution in the oxide particle.

According to the microstructural characterizations, the preliminary mechanisms of the PECJ process of ODS alloys can be proposed. The PEC joining process of ODS alloys can be divided into three steps that may occur simultaneously (**Figure 6**). The step (I) is the sintering of mechanical alloying powders in the joint area. The mechanical alloying powders loaded between the ODS base alloys were consolidated through solid-state sintering process by the pulsed electron current during the PECJ process. In addition to Joule heating, the intrinsic role of electrical current on the powder sintering process may involve several possible mechanisms, including plasma generation [34], electromigration [35], or dielectric breakdown of the surface oxide film [36]. The plasma generation theory proposed the formation of spark discharge and plasma through the ionization of gas between the powders, which can activate the sintering process [37, 38]. However, whether plasma can be formed has been questioned by the recent experimental investigations [39]. The insulating oxide films on the surface of metal powders, which are usually several nanometres thick and formed by oxidation in the air [40], can affect the kinetics of neck formation and growth during the initial stage of sintering. Chaim suggested that the enhanced surface conductivity with rising temperatures can promote electric field intensification at the inter-particle contact areas, resulting in electric field induced dielectric breakdown of surface oxide films [40]. Wang *et al.* investigated the electric field assisted sintering (EFAS) of stainless steel 316L nanoparticles using *ex situ* and *in situ* electron microscopy experiments, which suggested the sintering of stainless steel nanoparticles may experience four stages: the initial electric current cleaning of the oxide film, subsequent neck formation, neck growth, and the final fast consolidation [40]. Due to the similarity of the compositions of ODS 304 steels and 316L stainless steels, the similar EFAS mechanisms may be applied to the step (I), i.e., sintering of powders. In addition to the electrical current, the applied pressure may also have an intrinsic effect to increase the driving forces for sintering, as well as the extrinsic effects on the particle rearrangement and the destruction of agglomerates in powders to accelerate the densification of powders [41–43]

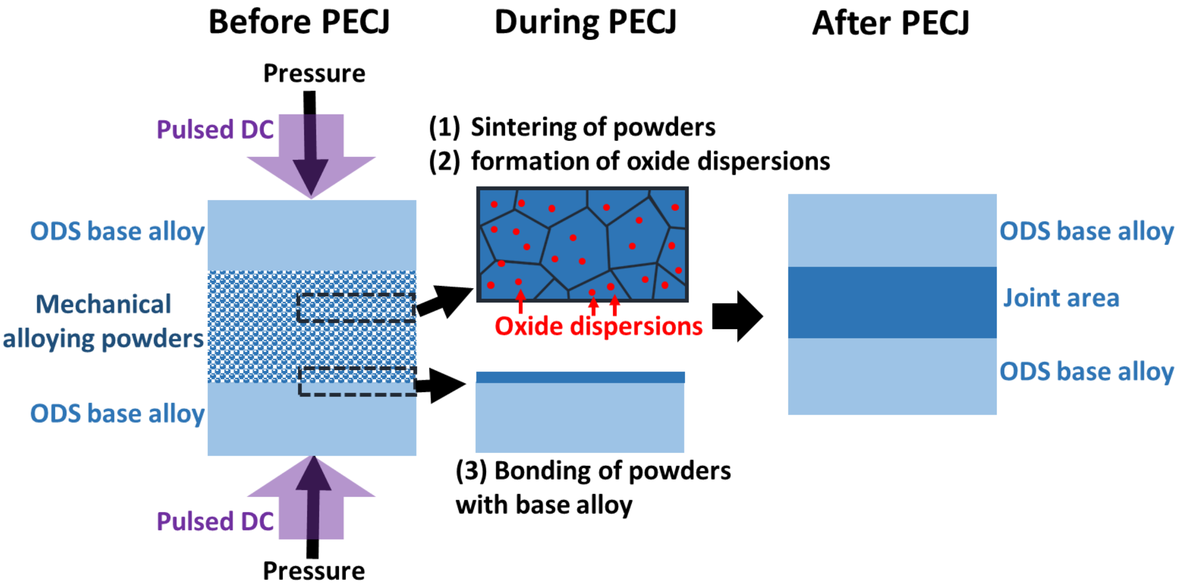

Fig. 6. The proposed mechanism of PECJ process of ODS alloys.

The step (II) is the formation of oxide dispersions inside the bonding layer, which mainly involves the crystallization of oxide dispersion particles from the amorphous oxygen-rich regions formed by mechanical alloying. The formation mechanisms of oxygen-enriched precipitates in ODS alloys have been studied for years. Recent experimental studies suggest that the originally added Y_2O_3 powders are dissolved during ball milling, and then the oxygen-enriched nanoparticles precipitate during the heating procedure [44–46]. Hsiung *et al.* suggest that the precipitation of oxide dispersions initiates from the amorphous oxygen-rich regions formed during ball milling, as a consequence of the diffusion of dissolved Y_2O_3 as well as those metal elements that have a high affinity for oxygen such as Ti [47]. Williams *et al.* [44] reported that the amorphous Y-Ti-O clusters were less than 1 nm after mechanical alloying, which are crystallized to nanoparticles and grow considerably during the heating process. These mechanisms may be applied to the formation of oxide dispersions in the joint area during the step (II) of the PECJ process of ODS alloys.

The step (III) is the bonding of the mechanical alloying powders with the base alloy, which may be influenced by the contact resistance and mass transport at their interface. The interface between the powders and the base alloy has higher electrical resistance than the base alloy, due to the small contact area and the insulating oxide films on the surface of metal powders. The high contract resistance can lead to Joule heating between the powders and bulk. It is also possible that an enhanced mass transport can occur at the interface through the electromigration mechanism of the electrical field. The electromigration theory suggests that the increase in the flux of the diffusion of atoms is a result of the momentum transfer from an "electron wind" effect [48]. Bertolino *et al*. [49, 50] revealed that in the Au-Al multilayer systems, the electromigration increased the rate of product layer formation and decreased the incubation time for the nucleation of a new phase. Thus, both high contact resistance and electromigration may be contributed to the formation of the solid-state bonding at the interface between the powders and base alloy during the step (I) the PECJ process of ODS alloys.

The distribution of microhardness along the cross-section of PECJ samples of ODS 304 austenitic steels was measured by Vickers indentations (**Fig. 7**). The microhardness in the base alloy and joint area formed for 3 min was 4.03±0.05 GPa and 3.88±0.10 GPa, respectively. The joint area had a slightly lower hardness and higher standard error. By lengthening the holding time to 10 min, the microhardness in the joint area had considerable variations and dropped 9.4% from 4.06±0.15 to 3.68±0.21 GPa on average compared to the base alloy. The microhardness decrease in the joint area formed for 10 min correlated with the coarsening of oxide dispersions (Fig. 4c), suggesting that the coarsening of oxide dispersions may lead to the degradation of mechanical properties of ODS alloy joints. The standard error of hardness in the joint area was higher than that of the base alloy, suggesting a greater variation in grain size or oxide dispersions in the joint area.

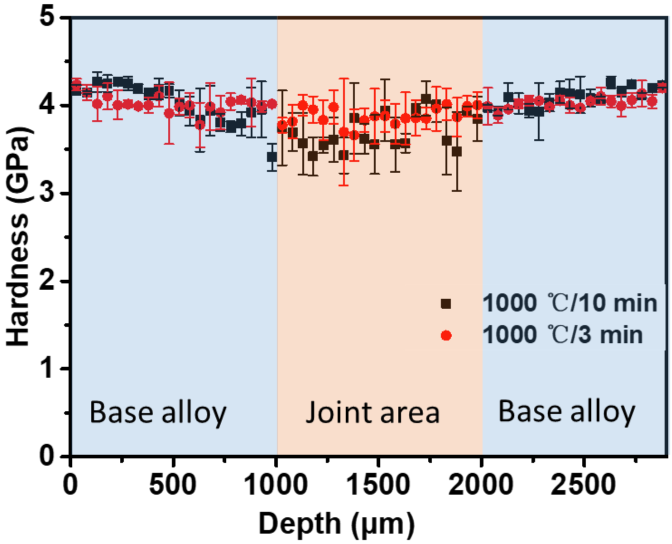

Fig. 7. Vickers microhardness along the cross-section of the PECJ samples of ODS 304 austenitic steels prepared at 1000 ºC and 50 MPa with a holding time of 3 min and 10 min, respectively.

For a preliminary evaluation of irradiation damage behavior in PECJ samples of ODS 304 austenitic steels (1000 ºC, 50 MPa, 3 min holding time), 2.8 MeV Au^{4+} ions were used to *in situ* irradiate the TEM samples at room temperature. After Au^{4+} ion irradiation to 3.5 dpa, there was no change in the size or morphology of the oxide dispersions. A large number of dislocation loops were generated in the austenitic steel matrix, and many of them were annihilated at the dispersion/matrix interface. For example, **Fig. 8a** and **Fig. 8b** are two successive dark-field TEM images with a time interval of 300 ms near 2.1 dpa, which showed one typical case that a dislocation loop was annihilated at the dispersion/matrix interface. The annihilation behavior indicated that the dispersion/matrix interfaces in the PECJ samples were still effective sinks for irradiation defects. Statistical analysis showed that the mean size of dislocation loops remained nearly the same (~ 2 nm) with the irradiation dose from 0 to 3.5 dpa (**Fig. 8c**), while the number density of dislocation loops increased less than one order (**Fig. 8d**). Although no control sample of ODS base alloy was used in the irradiation experiment for the direct comparison, the absence of the coarsening of dislocation loops (Fig. 7c) indicated the growth of dislocation loops might be suppressed by the sinks of dispersion/matrix interfaces that can annihilate point defects and promote the recombination of vacancies and interstitials [51, 52]. The dislocation loop density

($1.2\times10^{22}/m^3$) of the joint area at 1 dpa is similar to the loop density ($1.5\times10^{22}/m^3$) reported by Yan et al. in the study of irradiation behavior of ODS 304 steels at 1 dpa by 1 MeV Kr ions [53]. These results suggest that the PECJ samples of ODS 304 austenitic steels retained a high irradiation resistance.

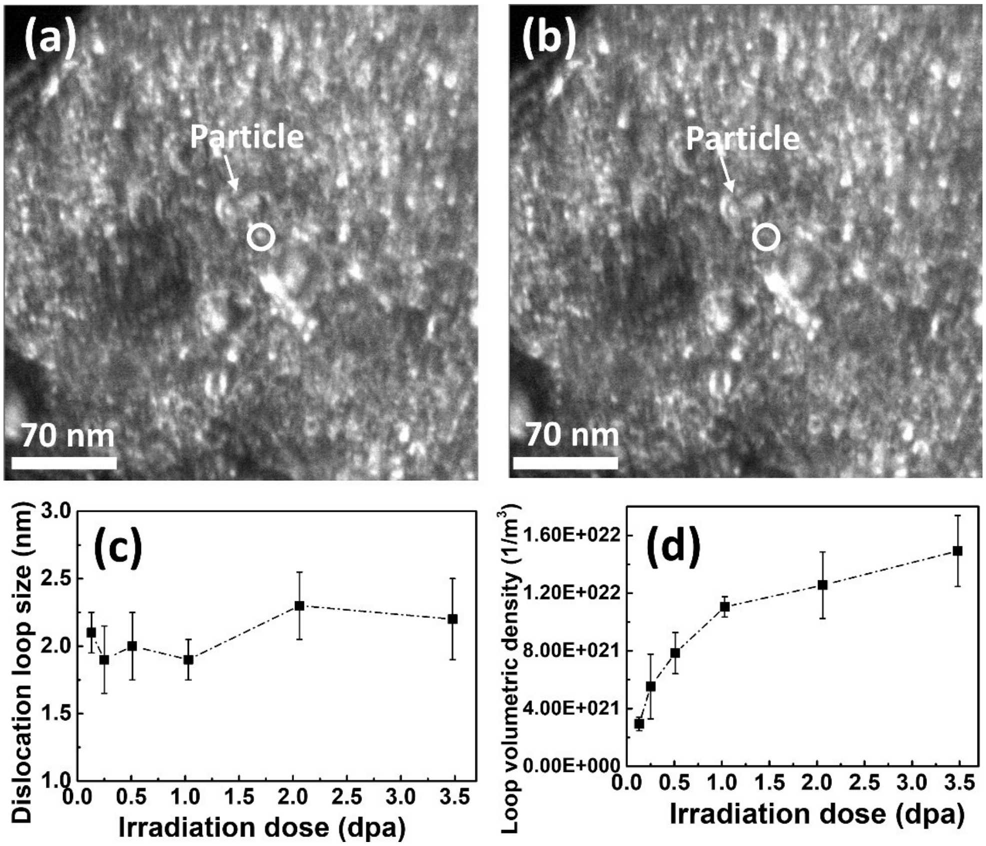

Fig. 8. (a, b) Dark-field TEM images of the joint area, showing a dislocation loop (indicated by the circle), disappeared at the dispersion/matrix interface at 2.1 dpa during 2.8 MeV Au^{4+} ion irradiation at room temperature. (c) Mean size and (d) volumetric density of dislocation loops as a function of irradiation dose.

4. Conclusion

A solid-state joining of ODS austenitic steels can be successfully formed by the PECJ process at 1000 °C and 50 MPa. SEM and EBSD characterizations suggested negligible grain growth in austenitic grain structures. TEM analysis showed the oxide dispersion particles in the joint area were still finely and uniformly dispersed, with slight coarsening of oxide dispersions at a short holding time of 3 min. The proposed mechanisms of the PECJ process of ODS alloys may be divided into three steps that may occur simultaneously, including the sintering of mechanical alloying powders in the bonding layer, formation of oxide dispersions, and bonding of the mechanical alloying powders with the base alloy. The microhardness of the joint areas was also close to that of the base alloy at a short holding time. *In situ* ion-irradiation experiments suggested that the irradiation resistance was retained in the jointed area due to the sink effect of oxide dispersions. Because of these benefits, the PECJ process is demonstrated to be a promising technology for the advanced manufacturing of ODS alloys for nuclear and fossil energy applications.

Acknowledgments

This work supported by the National Science Foundation under Grant No. CMMI-1762190. B. Cui acknowledges the Nuclear Regulatory Commission Faculty Development Grant (No. 31310018M0045). The research was performed in part in the Nebraska Nanoscale Facility:

National Nanotechnology Coordinated Infrastructure and the Nebraska Center for Materials and Nanoscience (and/or NERCF), which are supported by the National Science Foundation under Award ECCS: 2025298, and the Nebraska Research Initiative. This work was performed, in part, at the Center for Integrated Nanotechnologies, an Office of Science User Facility operated for the U.S. Department of Energy (DOE) Office of Science. Sandia National Laboratories is a multimission laboratory managed and operated by National Technology & Engineering Solutions of Sandia, LLC, a wholly owned subsidiary of Honeywell International, Inc., for the U.S. DOE's National Nuclear Security Administration under contract DE-NA-0003525. The views expressed in the article do not necessarily represent the views of the U.S. DOE or the United States Government.

Declaration of interest – the authors declare that they have no conflict of interest.

References

1. Chen W-Y, Miao Y, Wu Y, et al (2015) Atom probe study of irradiation-enhanced α′ precipitation in neutron-irradiated Fe–Cr model alloys. J Nucl Mater 462:242–249

2. Miao Y, Mo K, Zhou Z, et al (2016) Size-dependent characteristics of ultra-fine oxygen-enriched nanoparticles in austenitic steels. J Nucl Mater 480:195–201

3. Yan X, Zhang X, Wang F, et al (2019) Fabrication of ODS austenitic steels and CoCrFeNi high-entropy alloys by spark plasma sintering for nuclear energy applications. JOM 71:2856–2867

4. Zinkle SJ, Boutard JL, Hoelzer DT, et al (2017) Development of next generation tempered and ODS reduced activation ferritic/martensitic steels for fusion energy applications. Nucl Fusion 57:092005

5. Aydogan E, Maloy SA, Anderoglu O, et al (2017) Effect of tube processing methods on microstructure, mechanical properties and irradiation response of 14YWT nanostructured ferritic alloys. Acta Mater 134:116–127

6. Stan T, Wu Y, Ciston J, et al (2020) Characterization of polyhedral nano-oxides and helium bubbles in an annealed nanostructured ferritic alloy. Acta Mater 183:484–492

7. Hoelzer DT, Massey CP, Zinkle SJ, et al (2020) Modern nanostructured ferritic alloys: A compelling and viable choice for sodium fast reactor fuel cladding applications. J Nucl Mater 529:151928

8. Alam ME, Pal S, Maloy SA, Odette GR (2017) On delamination toughening of a 14YWT nanostructured ferritic alloy. Acta Mater 136:61–73. https://doi.org/10.1016/j.actamat.2017.06.041

9. Miao Y, Mo K, Zhou Z, et al (2015) On the microstructure and strengthening mechanism in oxide dispersion-strengthened 316 steel: A coordinated electron microscopy, atom probe tomography and in situ synchrotron tensile investigation. Mater Sci Eng A 639:585–596

10. Miao Y, Mo K, Cui B, et al (2015) The interfacial orientation relationship of oxide nanoparticles in a hafnium-containing oxide dispersion-strengthened austenitic stainless steel. Mater Charact 101:136–143

11. Gräning T, Rieth M, Hoffmann J, Möslang A (2017) Production, microstructure and mechanical properties of two different austenitic ODS steels. J Nucl Mater 487:348–361

12. Yan X, Wang F, Deng L, et al (2018) Effect of laser shock peening on the microstructures and properties of oxide-dispersion-strengthened austenitic steels. Adv Eng Mater 20:1700641

13. Oka H, Watanabe M, Hashimoto N, et al (2013) Morphology of oxide particles in ODS austenitic stainless steel. J Nucl Mater 442:S164–S168

14. Oka H, Watanabe M, Kinoshita H, et al (2011) In situ observation of damage structure in ODS austenitic steel during electron irradiation. J Nucl Mater 417:279–282

15. Leo JRO, Barroso SP, Fitzpatrick ME, et al (2019) Microstructure, tensile and creep properties of an austenitic ODS 316L steel. Mater Sci Eng A 749:158–165

16. Yan X, Wang F, Hattar K, et al (2019) Novel amorphous SiOC dispersion-strengthened austenitic steels. Materialia 6:100345

17. Odette GR, Alinger MJ, Wirth BD (2008) Recent Developments in Irradiation-Resistant Steels. Annu Rev Mater Res 38:471–503. https://doi.org/10.1146/annurev.matsci.38.060407.130315

18. Wright IG, Tatlock GJ, Badairy H, Chen CL (2009) Summary of Prior Work on Joining of Oxide Dispersion-Strengthened Alloys. Oak Ridge National Laboratory

19. Cvecek K, Dehmel S, Miyamoto I, Schmidt M (2019) A review on glass welding by ultra-short laser pulses. Int J Extreme Manuf 1:042001. https://doi.org/10.1088/2631-7990/ab55f6

20. Molian PA, Yang YM, Patnaik PC (1992) Laser welding of oxide dispersion-strengthened alloy MA754. J Mater Sci 27:2687–2694

21. McKimpson MG, O'Donnell D (1994) Joining ODS materials for high-temperature applications. JOM 46:49–51

22. Kasuga M, Sano T, Hirose A (2019) Grain refining in weld metal using short-pulsed laser ablation during CW laser welding of 2024-T3 aluminum alloy. Int J Extreme Manuf 1:045003. https://doi.org/10.1088/2631-7990/ab563a

23. Baker BW, Brewer LN (2014) Joining of oxide dispersion strengthened steels for advanced reactors. Jom 66:2442–2457

24. Mathon MH, Klosek V, De Carlan Y, Forest L (2009) Study of PM2000 microstructure evolution following FSW process. J Nucl Mater 386:475–478

25. Legendre F, Poissonnet S, Bonnaillie P, et al (2009) Some microstructural characterisations in a friction stir welded oxide dispersion strengthened ferritic steel alloy. J Nucl Mater 386:537–539

26. Lear CR, Eftink BP, Lienert TJ, Maloy SA (2019) Capacitive Discharge Resistance Welding for ODS Steel Cladding: Weld Properties and Radiation Resistance. Los Alamos National Lab.(LANL), Los Alamos, NM (United States)

27. Nishimoto K, Saida K, Tsuduki R (2004) In situ sintering bonding of oxide dispersion strengthened superalloys using pulsed electric current sintering technique. Sci Technol Weld Join 9:493–500

28. Tatlock GJ, Dyadko EG, Dryepondt SN, Wright IG (2007) Pulsed Plasma-Assisted Diffusion

Bonding of Oxide Dispersion-Strengthened–FeCrAl Alloys. Metall Mater Trans A 38:1663–1665

29. Fu H, Nagasaka T, Muroga T, et al (2015) Weldability of 9Cr-ODS and JLF-1 Steels for Dissimilar Joining with Hot Isostatic Pressing and Electron Beam Welding. Plasma Fusion Res 10:3405015–3405015. https://doi.org/10.1585/pfr.10.3405015

30. Hattar K, Bufford DC, Buller DL (2014) Concurrent in situ ion irradiation transmission electron microscope. Nucl Instrum Methods Phys Res Sect B Beam Interact Mater At 338:56–65

31. Stoller RE, Toloczko MB, Was GS, et al (2013) On the use of SRIM for computing radiation damage exposure. Nucl Instrum Methods Phys Res Sect B Beam Interact Mater At 310:75–80

32. Jiang S, Horn TJ, Dhir VK (2000) Numerical Analysis of a Radiant Heat Flux Calibration System. Int J Thermophys 21:941–963. https://doi.org/10.1023/A:1006622526578

33. Wang F, Zhou Q, Li X-Z, et al (2021) Electron microscopy observation of electric field-assisted sintering of stainless steel nanoparticles. J Mater Sci 56:2584–2596. https://doi.org/10.1007/s10853-020-05348-1

34. Munir ZA, Anselmi-Tamburini U, Ohyanagi M (2006) The effect of electric field and pressure on the synthesis and consolidation of materials: A review of the spark plasma sintering method. J Mater Sci 41:763–777

35. Munir ZA, Quach DV, Ohyanagi M (2011) Electric current activation of sintering: a review of the pulsed electric current sintering process. J Am Ceram Soc 94:1–19

36. Orru R, Licheri R, Locci AM, et al (2009) Consolidation/synthesis of materials by electric current activated/assisted sintering. Mater Sci Eng R Rep 63:127–287

37. Marder R, Estournès C, Chevallier G, Chaim R (2014) Plasma in spark plasma sintering of ceramic particle compacts. Scr Mater 82:57–60

38. Zhang Z-H, Liu Z-F, Lu J-F, et al (2014) The sintering mechanism in spark plasma sintering–proof of the occurrence of spark discharge. Scr Mater 81:56–59

39. Hulbert DM, Anders A, Andersson J, et al (2009) A discussion on the absence of plasma in spark plasma sintering. Scr Mater 60:835–838

40. Wang F, Zhou Q, Li X-Z, et al (2021) Electron microscopy observation of electric field-

assisted sintering of stainless steel nanoparticles. J Mater Sci 56:2584–2596. https://doi.org/10.1007/s10853-020-05348-1

41. Munir ZA, Anselmi-Tamburini U, Ohyanagi M (2006) The effect of electric field and pressure on the synthesis and consolidation of materials: A review of the spark plasma sintering method. J Mater Sci 41:763–777

42. Makino Y, Sakaguchi M, Terada J, Akamatsu K (2007) Consolidation of Ultrafine Alumina Powders with SPS Method. 粉体および粉末冶金 54:219–225. https://doi.org/10.2497/jjspm.54.219

43. Zhang X, Khedmati M, Kim Y-R, et al (2020) Microstructure evolution during spark plasma sintering of FJS-1 lunar soil simulant. J Am Ceram Soc 103:899–911

44. Williams CA, Unifantowicz P, Baluc N, et al (2013) The formation and evolution of oxide particles in oxide-dispersion-strengthened ferritic steels during processing. Acta Mater 61:2219–2235. https://doi.org/10.1016/j.actamat.2012.12.042

45. Brocq M, Radiguet B, Poissonnet S, et al (2011) Nanoscale characterization and formation mechanism of nanoclusters in an ODS steel elaborated by reactive-inspired ball-milling and annealing. J Nucl Mater 409:80–85

46. Yamashita* S, Ohtsuka S, Akasaka N, et al (2004) Formation of nanoscale complex oxide particles in mechanically alloyed ferritic steel. Philos Mag Lett 84:525–529

47. Hsiung LL, Fluss MJ, Tumey SJ, et al (2010) Formation mechanism and the role of nanoparticles in Fe-Cr ODS steels developed for radiation tolerance. Phys Rev B 82:184103

48. Heersche HB, Lientschnig G, O’Neill K, et al (2007) In situ imaging of electromigration-induced nanogap formation by transmission electron microscopy. Appl Phys Lett 91:072107

49. Bertolino N, Garay J, Anselmi-Tamburini U, Munir ZA (2001) Electromigration effects in Al-Au multilayers. Scr Mater 44:737–742

50. Bertolino N, Garay J, Anselmi-Tamburini U, Munir ZA (2002) High-flux current effects in interfacial reactions in Au–Al multilayers. Philos Mag B 82:969–985

51. Oka K, Ohnuki S, Yamashita S, et al (2007) Structure of nano-size oxides in ODS steels and its stability under electron irradiation. Mater Trans 48:2563–2566

52. Oka H, Watanabe M, Kinoshita H, et al (2011) In situ observation of damage structure in ODS austenitic steel during electron irradiation. J Nucl Mater 417:279–282

53. Yan X, Wang F, Deng L, et al (2018) Effect of Laser Shock Peening on the Microstructures and Properties of Oxide-Dispersion-Strengthened Austenitic Steels. Adv Eng Mater 20:1700641. https://doi.org/10.1002/adem.201700641

Figure Captions

Fig. 1. The schematic diagram of the pulsed electric current joining (PECJ) process of ODS alloys.

Fig. 2. The profiles of electrical voltage, current, resistance, pressure, and temperature during the PECJ process.

Fig. 3. SEM images of the cross-section of the PECJ samples of ODS 304 austenitic steels prepared at 1000 ºC and 50 MPa with a holding time of (a) 3 min and (b) 10 min. The vertical red arrows indicate the interfaces between the base metal and the joint. (a') and (b') are the enlarged view of the interface in (a) and (b).

Fig. 4. Typical EBSD images of (a) base alloy and the joint area with a holding time of (b) 3 min and (c) 10 min. (d)-(e) are grain size distributions corresponding to a to c, respectively.

Fig. 5. Representative bright-field TEM images of (a) base alloy and the joint areas with a holding time of (b) 3 min and (c) 10 min. (d)-(f) are the quantitative analysis of the particle size distribution and number densities of oxide dispersions corresponding to images a to c, respectively. (g) HAADF image of an oxide dispersion particle. (h)-(j) elements distribution in the oxide particle.

Fig. 6. The proposed mechanism of PECJ process of ODS alloys.

Fig. 7. Vickers microhardness along the cross-section of the PECJ samples of ODS 304 austenitic steels prepared at 1000 ºC and 50 MPa with a holding time of 3 min and 10 min, respectively.

Fig. 8. (a, b) Dark-field TEM images of the joint area, showing a dislocation loop (indicated by the circle), disappeared at the dispersion/matrix interface at 2.1 dpa during 2.8 MeV Au^{4+} ion irradiation at room temperature. (c) Mean size and (d) volumetric density of dislocation loops as a function of irradiation dose.

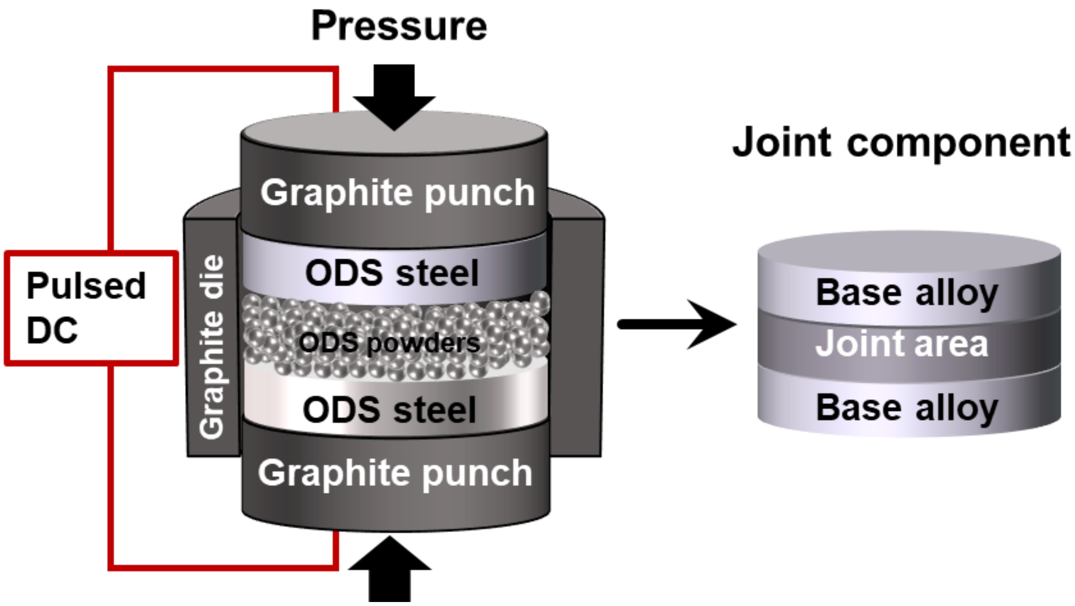

Fig. 1. The schematic diagram of the pulsed electric current joining (PECJ) process of ODS alloys.

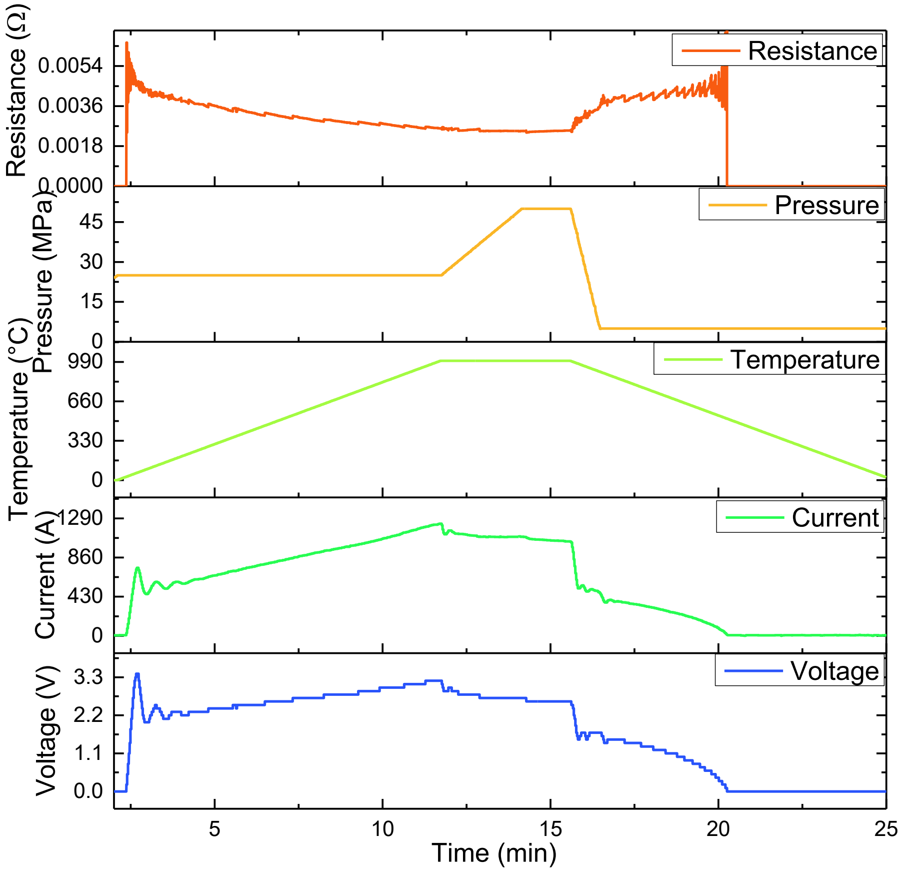

Fig. 2. The profiles of electrical voltage, current, resistance, pressure, and temperature during the PECJ process.

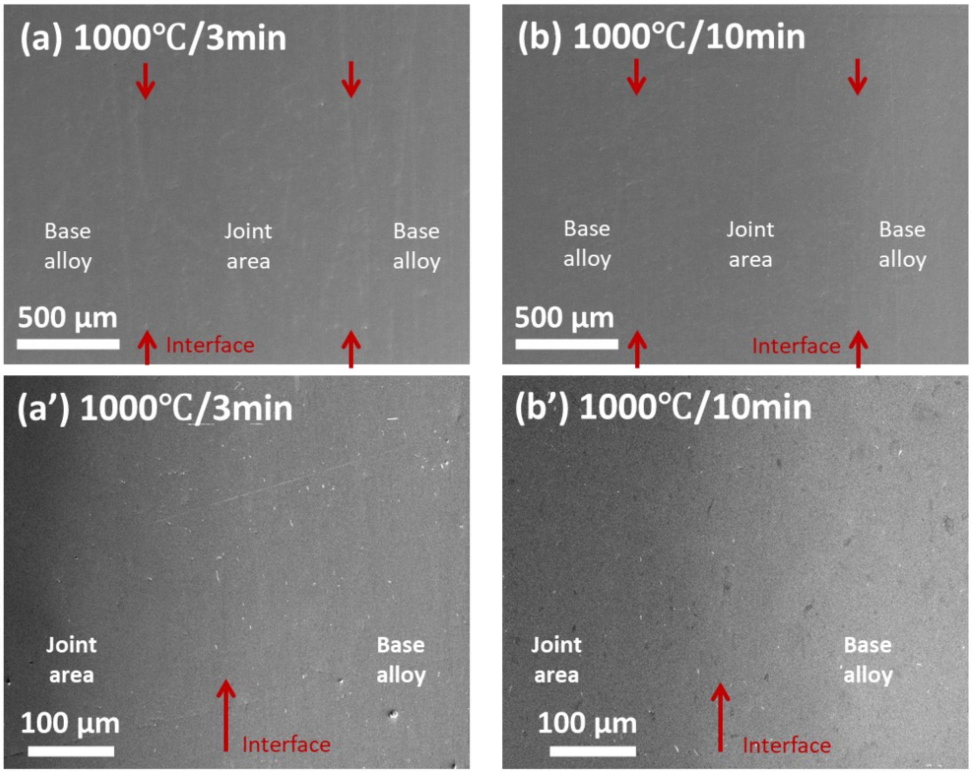

Fig. 3. SEM images of the cross-section of the PECJ samples of ODS 304 austenitic steels prepared at 1000 ºC and 50 MPa with a holding time of (a) 3 min and (b) 10 min. The vertical red arrows indicate the interfaces between the base metal and the joint. (a') and (b') are the enlarged view of the interface in (a) and (b).

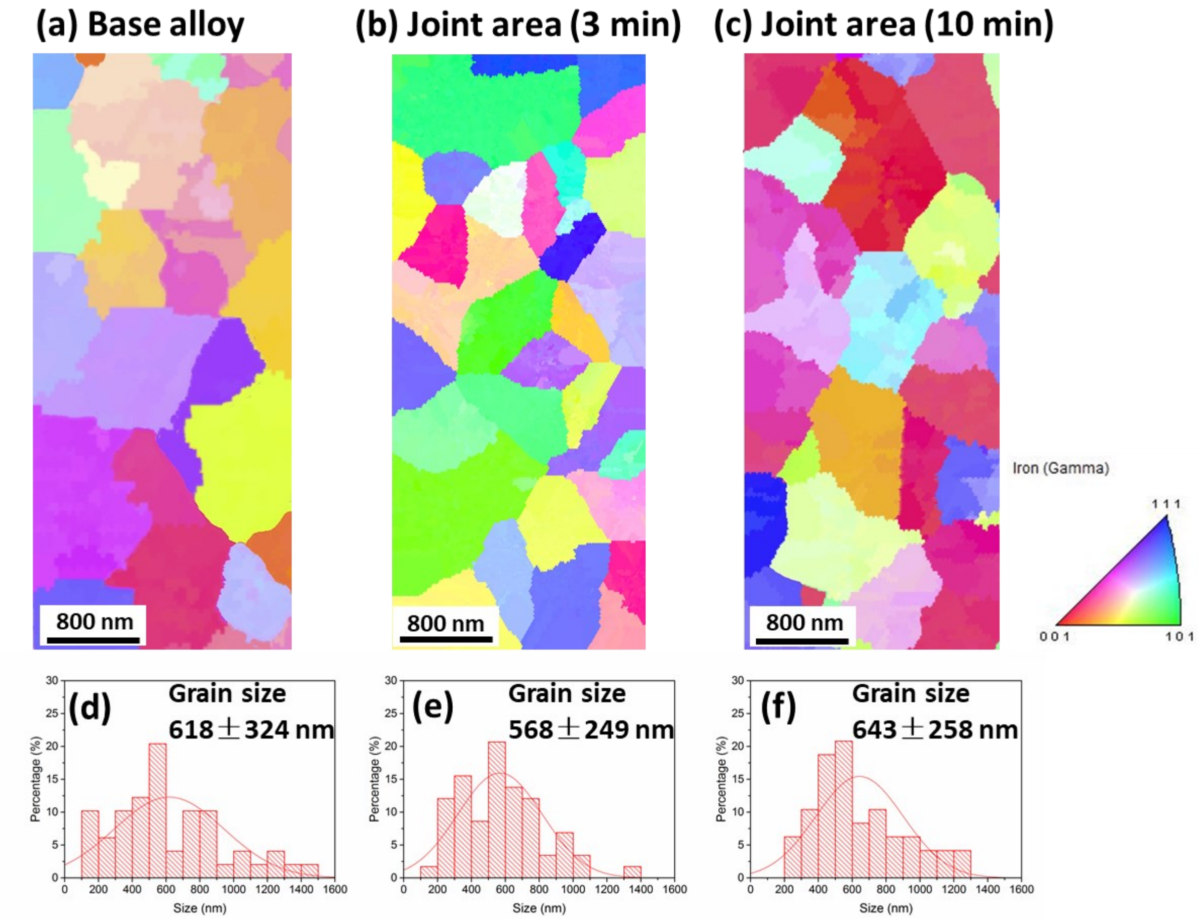

Fig. 4. Typical EBSD images of (a) base alloy and the joint area with a holding time of (b) 3 min and (c) 10 min. (d)-(e) are grain size distributions corresponding to a to c, respectively.

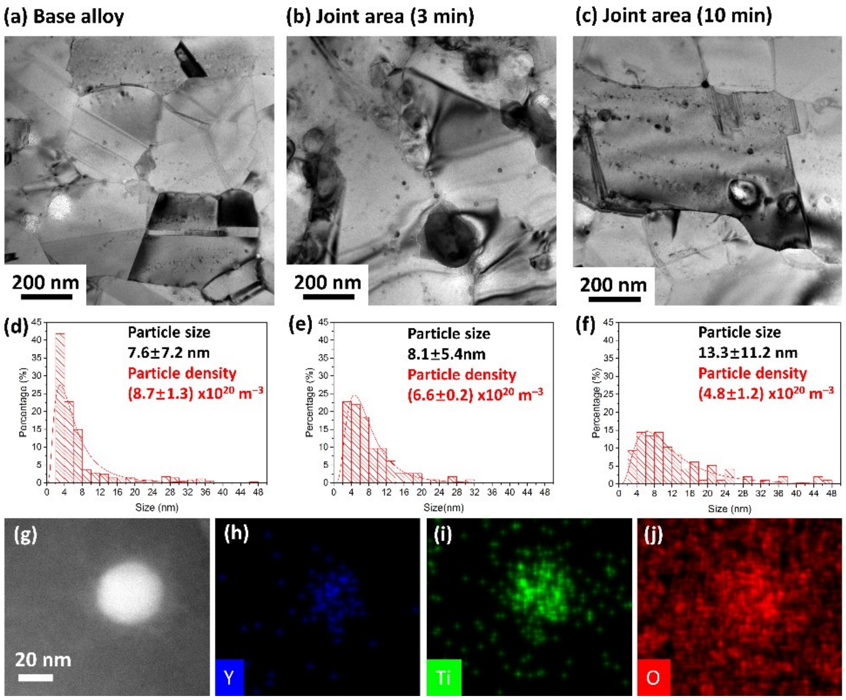

Fig. 5. Representative bright-field TEM images of (a) base alloy and the joint areas with a holding time of (b) 3 min and (c) 10 min. (d)-(f) are the quantitative analysis of the particle size distribution and number densities of oxide dispersions corresponding to images a to c, respectively. (g) HAADF image of an oxide dispersion particle. (h)-(j) elements distribution in the oxide particle.

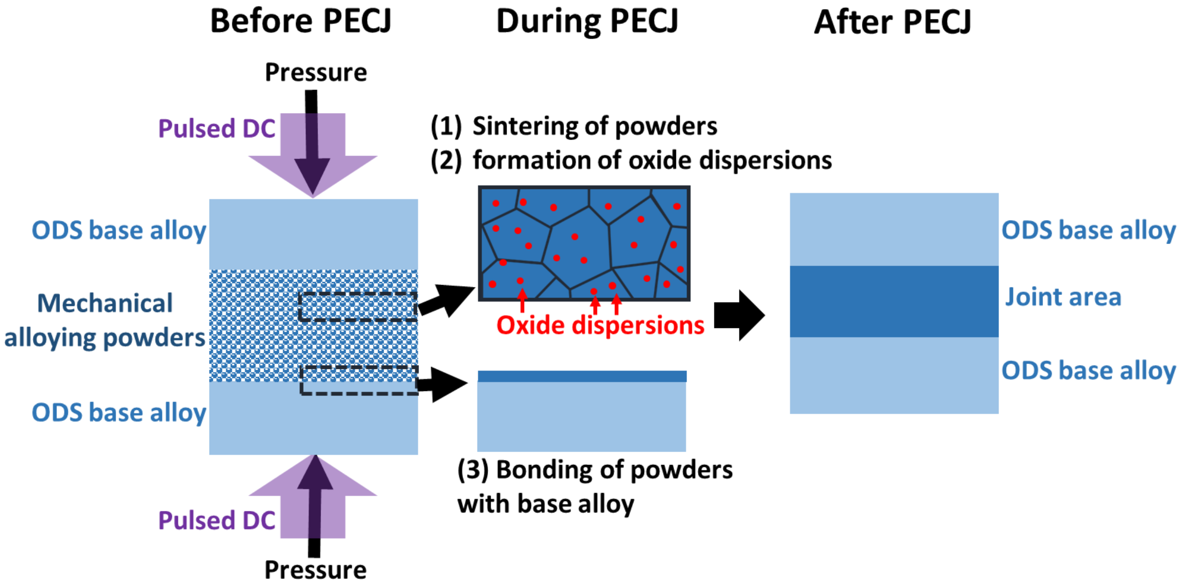

Fig. 6. The proposed mechanism of PECJ process of ODS alloys.

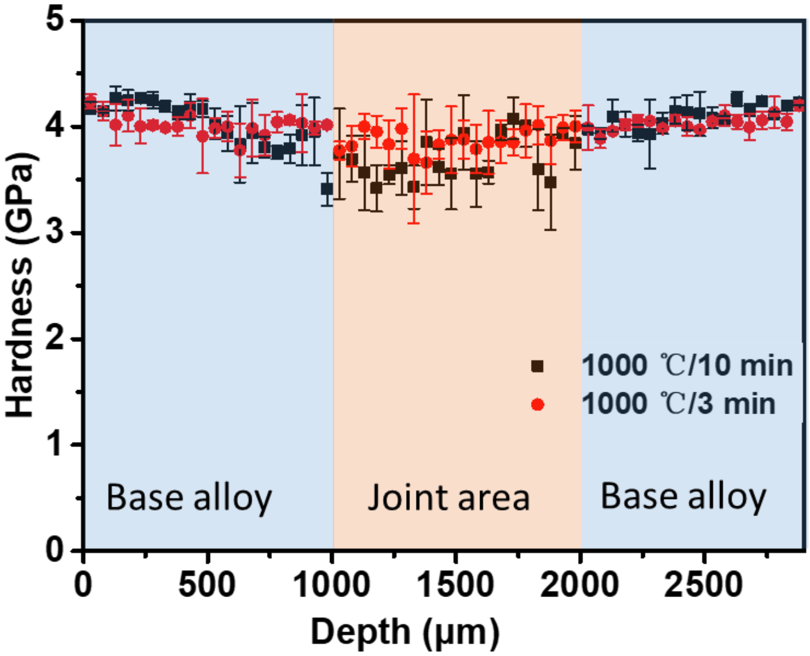

Fig. 7. Vickers microhardness along the cross-section of the PECJ samples of ODS 304 austenitic steels prepared at 1000 ºC and 50 MPa with a holding time of 3 min and 10 min, respectively.

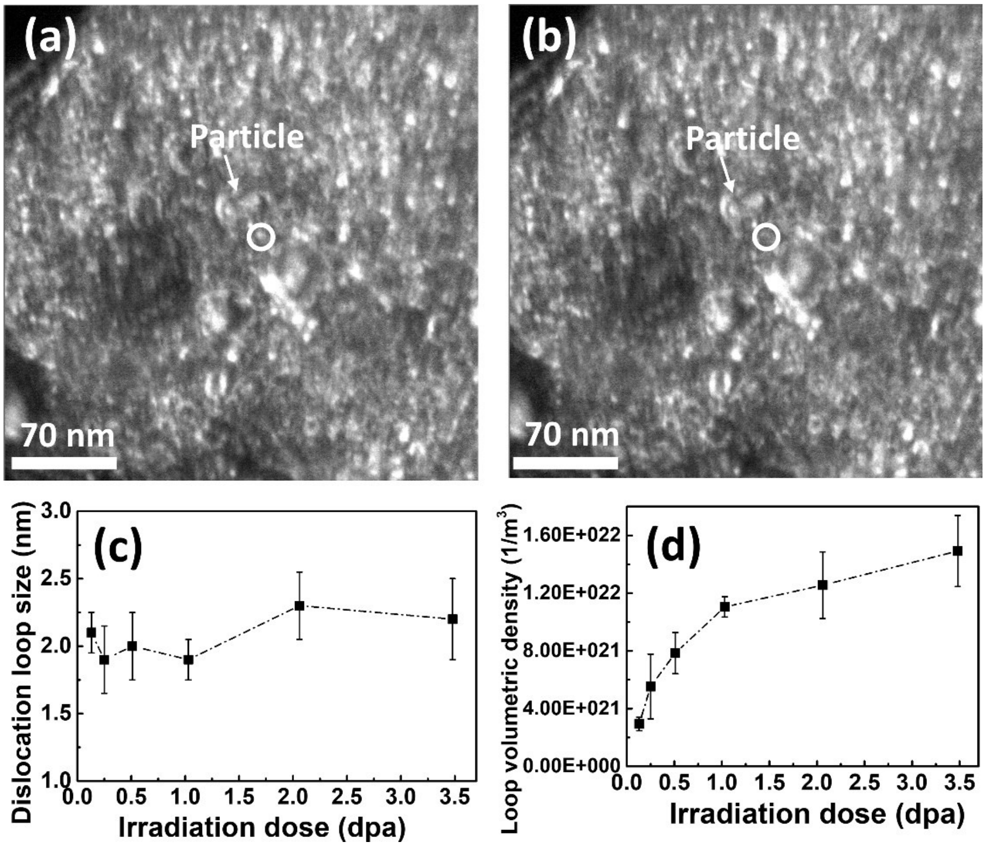

Fig. 8. (a, b) Dark-field TEM images of the joint area, showing a dislocation loop (indicated by the circle), disappeared at the dispersion/matrix interface at 2.1 dpa during 2.8 MeV Au^{4+} ion irradiation at room temperature. (c) Mean size and (d) volumetric density of dislocation loops as a function of irradiation dose.